Towards Optimizing Electrospun Nanofiber Fuel Cell Catalyst Layers: Polymer-Particle Interactions and Spinnability

Sunilkumar Khandavalli[1†], Nisha Sharma-Nene[1†], Sadia Kabir[1], Samrat Sur[2], Jonathan P. Rothstein[2], Kenneth C. Neyerlin[1], Scott Mauger[1] and Michael Ulsh[1]*

[1]Chemistry and Nanoscience Center, National Renewable Energy Laboratory, Golden, CO

80401, USA

[2]Mechanical and Industrial Engineering, University of Massachusetts, Amherst, MA 01003, USA

60439, USA

*E-mail: Michael.Ulsh@nrel.gov

Phone: +1 (303) 275 3842

[†] Authors contributed equally to this work.

Abstract

We investigate the effect of the poly(acrylic acid) (PAA) carrier polymer concentration on the microstructure and rheological properties of catalyst inks for electrospun polymer-electrolyte membrane fuel cell catalyst layers. Characterization of ink microstructure using oscillatory shear rheology showed the catalyst particles (platinum on carbon) are significantly agglomerated in the absence of PAA or ionomer. Both ionomer and PAA promoted the stability of the particles against agglomeration via electrosteric stabilization by adsorbing onto the particle surface. Increasing the PAA concentration increased the stability of the particles (or reduced the agglomerated structure) due to increasing PAA coverage onto the free surface area of the particles. However, beyond a certain increase in concentration, PAA was found to predominantly remain as excess free polymer in the ink due to insufficient free/available surface area on the particles for further PAA coverage. Extensional rheology measurements demonstrated that PAA enhances the extensional viscosities of the inks. Consequently, increasing the PAA concentration in the ink promoted the evolution of uniform nanofibers. However, beyond a certain concentration, significant increase in the shear viscosities of the inks led to defective fiber morphologies because of the onset of flow instabilities. Electrochemical performance comparisons between catalyst layers with different PAA concentrations showed maximum performance at PAA concentration that led to the least agglomerated structure of the catalyst, most uniform fiber morphologies, and low concentrations of free (non-adsorbing) PAA in the electrode. These results provide a rationale for optimization of electrospun catalyst nanofibers for both spinnability and electrochemical performance.

Keywords: Nanofibers, electrospinning, poly(acrylic acid), extensional rheology, fuel cells, catalyst inks

Introduction

Polymer electrolyte membrane (PEM) fuel cells have attracted tremendous interest as a clean-emissions, highly efficient power source for both stationary and mobile applications[1,2]. A PEM fuel cell generates electricity from the electrochemical reaction of H_2 and O_2 producing water as a byproduct. A critical component of fuel cells is the cathode catalyst layer, which includes the catalyst – most often platinum on carbon – and ionomer, where the electrochemical reactions occur. The structure of the catalyst layer, at several length scales, dictates the transport of reactants and products to-and-from the catalyst site, which affects the utilization of the catalyst, and thus the performance. Optimization of the catalyst layer microstructure for performance still remains as a significant challenge.

To improve fuel cell performance, several studies have explored various alternate catalyst layer morphologies [3–5] to the conventional catalyst-coating layers with random morphologies[2]. Electrospun nanofiber catalyst layer morphologies have recently attracted interest due to improved performance and durability compared to the conventional morphology[3,6–10]. These enhancements have been attributed to better dispersion of catalyst and ionomer phases, which maximizes the three-phase interaction (carbon-ionomer-catalyst interface) and thus increases catalyst utilization, and increased porosity (due to inter-fiber void fraction) that enhances the mass-transport properties of the catalyst layer[8,10,11].

Electrospinning is one of the common techniques to fabricate nanofiber catalyst layers. It allows fiber fabrication from a diverse set of materials and can produce fibers with a wide range of diameters[12,13]. In this method, the liquid formulation is pumped through a nozzle and stretched by applying a high voltage potential between the nozzle tip and a grounded collector. As electrostatic repulsion forces between the excess ions in the fluid overcome the fluid interfacial tension, a jet evolves from the conical-shaped reservoir (known as the Taylor cone) formed at the nozzle tip. The jet is significantly deformed or elongated by the electrostatic forces. As this jet approaches the grounded collector, it solidifies into fibers due to solvent evaporation[14].

Control of fiber uniformity as well as the fiber diameter in the electrospinning process is important for quality and/or performance in many applications, not limited to fuel cells. The stability of the jet during the electrospinning process strongly influences the evolution of the fiber morphology. Jet stability is governed by the balance of viscous, elastic, capillary, and inertial forces. These forces, and thus the evolution of the fiber morphology, are dictated by a combination of fluid properties (i.e. rheology,

interfacial tension, conductivity), process parameters (e.g. liquid flow rate, voltage), and ambient conditions (e.g. temperature, relative humidity). Among these, fluid rheology is known to significantly affect the jet stability, and thus evolution of the fiber morphology[15,16]. To obtain uniform fibers, the jet needs to be stable without breaking up into droplets due to capillary (surface tension) forces. Inertia due to the acceleration of the jet by electrostatic forces exacerbates the capillary break-up process[14]. Viscoelastic forces resist inertia and facilitate the formation of uniform fibers by delaying the break-up of the jet into droplets. Thus, increasing viscoelasticity of the fluid, by increasing polymer concentration or molecular weight of polymer solutions, for example, is found to promote the stability of the jet and facilitate the formation of uniform fibers[15,17,18].

The typical perfluorosulfonic acid ionomer that is used in the catalyst ink formulation is relatively low molecular weight (Mw ~ 200,000 g/mol) and does not impart sufficient elasticity to enable fiber formation.[19,20] To enable nanofiber formation, high molecular weight (Mw) polymer additives (e.g. polyacrylic acid, polyethylene oxide, polyvinylidene fluoride, and polyacrylonitrile), referred to as carrier polymers, are commonly added to the catalyst inks [3,6–8,21–23]. To fabricate uniform fibers, the concentration of the carrier polymer must be high enough that it provides sufficient elasticity to fabricate uniform fibers but not so much that it results in defective fibers due to flow instabilities caused by significant increase in the viscoelasticity of the inks[24,25]. Mostly importantly from a performance perspective, excess carrier polymer can negatively affect fuel cell performance. Interaction of the carrier polymer with the particles (catalyst/carbon) and the ionomer may reduce the three-phase (catalyst-ionomer-carbon) interface and inhibit full utilization of the catalyst[3,7,26]. Furthermore, excessive carrier polymer in the fiber may also reduce the overall porosity and hinder mass transport in the catalyst layer[26].

Polyacrylic acid (PAA) is one of the commonly used carrier polymers for the fabrication of nanofiber fuel cell catalyst layers for a variety of catalyst systems[7,21,27,28]. Previous studies have identified the optimal concentration of PAA in the inks to produce uniform fiber morphologies[25]. Researchers have also reported on the impact of PAA on performance, though at limited PAA concentrations (10 – 15 wt.% PAA w.r.t total solids, i.e. Nafion, PAA, and particles)[3,7]. Excessive PAA was found to reduce fuel cell performance by decreasing the ionic and electronic conductivity of the electrode[3,7]. However, systematic studies investigating how the concentration of PAA affects both the evolution of the fiber morphologies and the performance are scarce. Rheological properties, particularly extensional properties that dominate electrospinning process, play an important role in the evolution of fiber morphologies[18]. Understanding

of how the carrier polymer influences both the rheological properties and the ink microstructure provide insights into the evolution of fiber morphologies and the internal structure of the fibers, and thus on device performance. The interaction of the carrier-polymer with the catalyst and the concentration of carrier-polymer can strongly impact the ink microstructure, and in turn affect the internal distribution of the components in the fibers. However, we are unaware of any such studies. Such knowledge is critical for efficient optimization of the carrier polymer in the nanofiber electrodes[26,29].

In this paper, we investigate the effect of PAA concentration on the ink component interactions (particularly carrier-polymer – particle interactions), the ink microstructure, and rheological properties – particularly the extensional flow properties. The impact of these on fiber morphology and fuel cell performance has also been examined. Oscillatory shear rheology was used to characterize the ink microstructure. The study shows that PAA stabilizes the catalyst against agglomeration. Additionally, extensional rheology measurements show that PAA enhances the extensional viscosities of the inks. Consequently, increasing the PAA concentration promotes the evolution of uniform fibers; however, large PAA concentrations result in non-uniform fiber morphologies because of significant increase in the shear viscosities of the inks. A combination of, improved fiber uniformity, reduced agglomerated structure of the catalyst, and low concentrations of free/excess (non-adsorbing) PAA in the electrode maximized the device performance.

In a parallel study, we further investigate the impact of PAA concentration on the distribution of ionomer within the nanofiber microstructure. Electron microscopy and several electrochemical diagnostic techniques are used to link the intra-fiber distribution of ionomer to their electrochemical properties.[30]

Materials and sample preparation

Poly (acrylic acid) (Mw ≈ 450,000 g/mol, Sigma Aldrich) was used as the carrier polymer. The catalyst was 46.7 wt.% platinum (Pt) on Vulcan carbon (Pt-Vulcan) (TKK, TEC10V50E) and the ionomer dispersion was 1000 EW Nafion (D2020, Ion Power). The dispersion media is a 50:50 (w/w) mixture of isopropyl alcohol (IPA, Alfa Aesar) and deionized water (Milli-Q).

Inks were prepared by adding desired amounts of catalyst (10 wt.%) and ionomer (3.41 wt.% w.r.t solvent) from the 20 wt.% stock D2020 dispersion into the dispersion media in a 20 ml vial. The ink mixture was then dispersed by probe sonication for 2x10 s, followed by bath sonicating in an ice bath for 2 h. Next the desired amount of PAA, ranging from 0 to 4.76 wt.%, was added to the ink mixture from a stock PAA solution (7.5 wt.% PAA solution in a 2:1 IPA:H_2O w/w solvent mixture) and then was mixed using a magnetic stirrer for at least 72 h to homogenize the mixture. All the concentrations of particles and polymer presented throughout the manuscript are based on mass and the concentrations are w.r.t to the dispersion media evaluated as $100*m_a/(m_a+m_s)$ where m_a is particles or polymer mass and m_s is the mass of the dispersion media. The PAA concentration range in the inks with ionomer corresponds to solids loading between 2.30 to 22.7 wt.% which is evaluated as $100*m_{PAA}/(m_{catalyst} + m_{PAA} + m_{ionomer})$.

Experimental

Shear Rheology

Rheological measurements were performed using a stress-controlled rheometer (Thermo-Scientific HAAKE Mars 60 Rheometer) with a stainless-steel parallel-plate geometry (40 mm diameter) with a gap of 500 µm at 25 ˚C. A solvent-saturation trap was used in order to minimize any solvent evaporation during measurements. Prior to making measurements, the samples were preconditioned to erase any sample loading history on the microstructure by conducting a pre-shear at 500 s^{-1} for 60 s, and then allowed to rest for 60 s. The steady shear rheology measurements were performed by imposing a decreasing rate sweep with logarithmic spacing ranging from 500 to 0.05 s^{-1}. For dynamic-oscillatory-shear measurements, the same pre-shear protocol was followed as for steady shear. In the amplitude-sweep measurements, the frequency was fixed at 0.5 Hz and the strain amplitude was increased logarithmically from 0.0001 to 10.

Extensional Rheology

To characterize extensional rheology of the fluids, a Dripping onto Substrate Capillary Breakup Extensional Rheometry (CaBER-DoS) technique, that was used in *Sur and Rothstein, 2018*[31], was used (Figure S1). In CaBER-DoS, the liquid is dispensed by a syringe pump (KD Scientific) and a liquid bridge is formed between a glass substrate and a nozzle by allowing a drop of liquid to drip from the nozzle. The diameter of the nozzle was D = 800 μm and the volume flow rate was Q = 0.02 ml/min. An aspect ratio of $H_0/D = 3$, where H_0 is the height of the nozzle from the substrate, was selected to form an unstable liquid bridge as soon as the drip makes contact and spreads on the substrate. A high speed camera (Phantom-Vision optics, V-4.2) at a frame rate of 25,000 fps and resolution of 192x64 pixels (for most of the experiments) and a long range microscope lens (Edmund optics, 4.5x zoom) were used to record the capillary break-up process[32]. Filament diameter was measured from the diameter decay images using an edge detection algorithm (Edgehog, KU Leuven). Diameter values below 20 μm were not reported to minimize the resolution error (± 5μm).

The diameter decay data of the test fluid is used to calculate the extensional flow properties. The diameter decay data was fit using spline function and differentiated to calculate the extension rates as,

$$\dot{\epsilon} = -\frac{2}{R_{mid}(t)}\frac{dR_{mid}(t)}{dt} \quad (1)$$

where R_{mid} is radius at the mid-filament. The apparent extensional viscosity was then calculated as,

$$\eta_E = \frac{2\sigma}{\frac{dR_{mid}}{dt}} \quad (2)$$

where σ is interfacial tension, which was taken as ~ 24.3 mN/m, of the dispersion media (1:1 water : IPA mixture, w/w)[33]. For a Newtonian fluid, the radius of the fluid filament will decay linearly with time, $R_{mid(t)} \sim (t_b - t)$, to the final breakup at time t_b.[34,33] And for a viscoelastic fluid, characterized by an Oldroyd-B model with a relaxation time of λ_E, the radius will decay exponentially with time, $R_{mid(t)} \sim \exp(-t/3\lambda_E)$ resulting in a constant extension rate of $\dot{\epsilon} = 2/3\,\lambda_E$[35]. The extensional relaxation times were determined from exponential fit to the diameter decay. The extensional viscosity was then examined as a function of Hencky strain given as,

$$\epsilon = 2\,\ln\left(\frac{R_i}{R_{mid}(t)}\right) \quad (3)$$

where R_i is the radius of the syringe tip.

Electrospinning

A custom designed electrospinning system was used to fabricate nanofibers (Figure S2). The ink was pumped using a syringe pump (KDS100 Infusion Syringe Pump) into stainless-steel needle (22-gauge, inner radius R_0 = 0.21 mm) at a fixed flow rate of Q_o = 0.5 ml/hr. A high-voltage potential of 15 kV relative to the collector was applied at the needle tip. The collector was a stainless-steel rotating drum (100 rpm) covered with aluminum foil. The distance between the needle-tip and the collector was 10 cm. Experiments were conducted at room temperature (23± 2 ^{0}C) and at relatively humidity between 35 – 40%RH which was controlled within the environmental chamber of the electrospinning system.

Electron Microscopy

SEM was conducted using Hitachi 400 and FEI Quanta 600 instruments. Samples were gold sputtered at a current of 45 mA prior to measurements. The voltage and the working distance were 11 kV and 3 - 7 cm (depending on the magnification), respectively.

MEA Fabrication & Test Procedure

The catalyst nanofibers were electrospun onto Nafion NR211 membranes (IonPower) with a target Pt loading of 0.10 mgPt cm^{-2}. The Pt loadings of the nanofiber electrodes were determined by X-ray fluorescence spectroscopy (Fischerscope XDV-SDD, 50 kV, 50 W X-ray source). For each coated section, the loading was measured in at least five locations. The anodes were fabricated by ultrasonic spray coating Pt supported on high surface carbon (TKK, TEC10E50E) catalyst dispersed in deionized-water/nPA (62 wt.% water) with a 0.9 ionomer/catalyst (w/w) ratio and a 0.10 mgPt cm^{-2} loading. The catalyst coated membranes were sandwiched between two 5 cm^2 Freudenberg H23C8 gas diffusion layers at ~18% compression. These, along with polytetrafluoroethylene gaskets, were then placed between the flow fields and the bolts were tightened to 40 in-lbs. The membrane-electrode-assemblies were activated and

conditioned using our previously established break-in and voltage recovery protocols[22]. Pt electrochemically accessible surface area was determined by integrating the hydrogen underpotential deposition (HUPD) region obtained from cyclic voltammograms at 100% RH under H_2/N_2 sweeping from 0.05 to 1.2 V versus RHE at 100 mV/s. The factor used for converting HUPD charge to ECSA was 210 $\mu C\ cmPt^{-2}$. The test protocol involved measuring the I-V curves from 0.75 V to OCV in H_2/O_2 and 0.3 V to OCV in H_2/Air at 80°C, 2.580 kPa_{abs} cell pressure and 100% RH for 4 minutes per point (average of last 1 min used) in the anodic direction.

Results and discussion

The results and discussion section is presented as follows. First, we investigate the effect of PAA concentration on the catalyst ink microstructure using rheology. Next, we investigate the effect of PAA concentration on the extensional rheological properties. Then we present the processing behavior of the inks in the electrospinning process where the examine how the rheological properties influence the fiber morphologies. We conclude with the comparison of performance of the electrodes fabricated with different PAA concentrations in relation to the structure of the nanofibers and the ink microstructure.

Ink Microstructure

Effect of PAA and ionomer

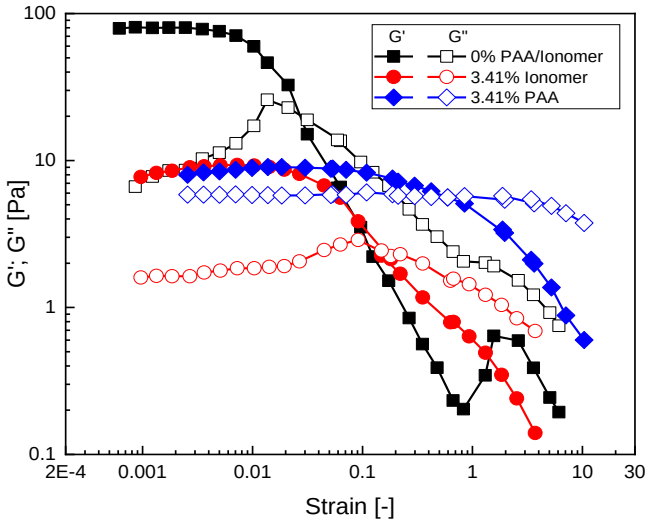

Figure 1. Amplitude-sweep measurements: elastic (G') and loss (G") moduli as a function of strain amplitude, for inks with no polymer, inks with PAA only, and inks with ionomer only.

We first investigated the effects of ionomer and PAA, independently, on the ink agglomerate structure, prior to examining the PAA concentration on the ink structure in the presence of ionomer. The amplitude sweep (AS) measurements of storage modulus (G') and loss modulus (G") as a function of strain amplitude (γ) of three ink cases are compared in Figure *1*. These include 1) neat inks (no polymer), inks with 2) ionomer and 3) PAA, both polymers at 3.41 wt.% concentration in the ink. The catalyst concentration in the inks was fixed at ~ 10 wt.% throughout the study. At low strains, where the moduli are independent of strain, i.e. the linear viscoelastic region, the storage moduli are greater than the loss moduli (G' > G") for all samples. This indicates their equilibrium structure is predominantly gel-like[36]. This also suggests the interparticle interactions are predominantly attractive and are leading to formation of a percolated-network-like (gel-like) structure[37]. As the strain amplitude is increased beyond the linear viscoelastic region, the moduli exhibit a cross-over (G' = G") and then decline with G' < G". This indicates a transition from a gel-like to a liquid-like structure. The decline in G' and G" at large strains, referred to as strain-softening and strain-thinning, respectively, indicates the break-down of the equilibrium percolated network of the particles/agglomerates by the deformation amplitudes.

If we compare the amplitude sweep response between the inks, both the magnitudes of the moduli in the linear viscoelastic region and the degree of non-linearity (strain-softening and strain-thinning) of the ink without any polymer are larger than the inks with polymer (ionomer or PAA). This indicates the strength of the gel-like structure (or the degree of percolation of the catalyst agglomerates), and thus the attraction strength between the particles, in the presence of ionomer or PAA is weaker compared to the inks without any polymer. Charged polymers can adsorb and stabilize the particles against van der Waals agglomeration via a well-known electro-steric stabilization mechanism, wherein a combination of both steric hinderance due to the coverage thickness and electrostatic repulsion associated with charged segments can provide inter-particle repulsion[38]. Both PAA and ionomer could be similarly inducing some stability to the particles, hence the reduced inter-particle attraction compared to ink with no polymer. This observation is also consistent with our previous rheological studies on the same Pt-Vulcan inks (though in the previous study, a water-1-propanol dispersion medium was used) where the ionomer significantly stabilized the agglomerated structure of the catalyst.[39]

Effect of PAA concentration at fixed ionomer content

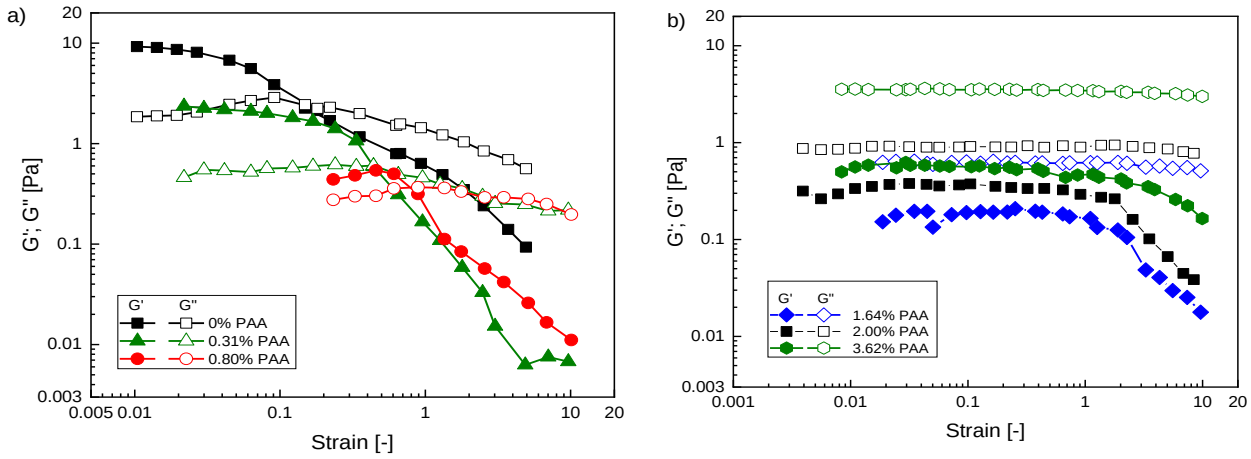

Figure 2. Amplitude-sweep measurements: elastic (G') and loss (G") moduli as a function of strain amplitude for inks with fixed ionomer concentration (3.41 wt%) for a series of PAA concentrations: a) 0 – 0.80 wt% and b) 1.64 - 3.62 wt%.

Next, we examined the effect of PAA concentration on the ink structure with a fixed ionomer concentration of 3.41 wt.%, which provides an ionomer/catalyst(Pt) mass ratio (I/C) of ~ 0.6, which is empirically considered to be optimal for the performance of dispersion-cast Pt-Vulcan catalyst layers[40]. Amplitude sweep measurements conducted on inks with PAA concentrations ranging from 0.31 to 3.62 wt.% are shown in Figure *2*a and *Figure* 2*b*. With increasing PAA, the amplitude response of the inks progressively changes from that of predominantly gel-like structure to a predominantly liquid-like structure. These changes as a function of PAA concentration can be better visualized by the trend in the moduli values in the linear viscoelastic region and their ratio, given by tan δ = G"/G' (Figure S3a in Supporting Information, SI). Their moduli values decreased initially until a PAA of ~ 0.80 wt.% and then increase with further increase in PAA. The tan δ also was found to change from ~ 0.2 to 6.6 with increasing PAA wt.% from 0 to 4.76 wt.%, indicating that the ink microstructure progressively changes from gel-like (tan $\delta < 1$) to liquid-like (tan $\delta > 1$) with a transition between 0.80 wt.% and 1.64 wt.%. The magnitude of strain-softening and strain-thinning behaviors were also characterized by the exponents, n_1 and n_2, respectively, which were obtained from power-law fits to the data as $G' \sim \gamma^{-n1}$ and $G'' \sim \gamma^{-n2}$ (Figure S3b in SI). Both n_1 and n_2, and thus the magnitude of strain-softening and strain-thinning, respectively, decreased with increasing PAA wt.%, though the decrease was more significant for the former than the latter. This trend suggests the degree of the agglomerated structure in the ink is decreasing with PAA concentration, consistent with the trend of tan δ in the linear viscoelastic region.

The amplitude sweep results indicate that PAA is progressively stabilizing the agglomerated structure of the particles, beyond what was imparted by the ionomer itself. The transition from a gel-like to a liquid-like structure, where the percolated network of the particle agglomerates is broken into isolated agglomerates/aggregates, occurs for PAA concentration between 0.80 wt.% and 1.64 wt.%. The increasing trend in the moduli (in the linear viscoelastic region) for PAA concentrations beyond 1.64 wt.% suggests that the rheological response is dominated by the increasing polymer concentration in the ink, even though some fraction of PAA seems to continue to stabilize/reduce the remaining agglomerates (as was evident from Figure S3b). The added polymer contributes to the total solids volume fraction in the inks, increasing their viscoelasticity. This behavior indicates that a significant fraction of the added PAA is remaining as free/excess polymer in the dispersion media for concentrations beyond 1.64 wt.%.

The above observations show that PAA is indeed interacting with the particles (Pt or carbon), more significantly at low PAA concentration (< 1.64 wt.%), and not remaining as an inert carrier in the ink.

Such interaction is reducing the agglomerated structure of the particles in the inks. At higher concentration, PAA appears to be predominantly remaining as free polymer in the ink. These changes in particle agglomeration and the amount of free polymer in the ink are likely to impact the catalyst utilization and mass transport properties of the catalyst layer. The implications of the ink microstructure on the fiber structure and the performance will be examined in later sections.

Extensional Rheology

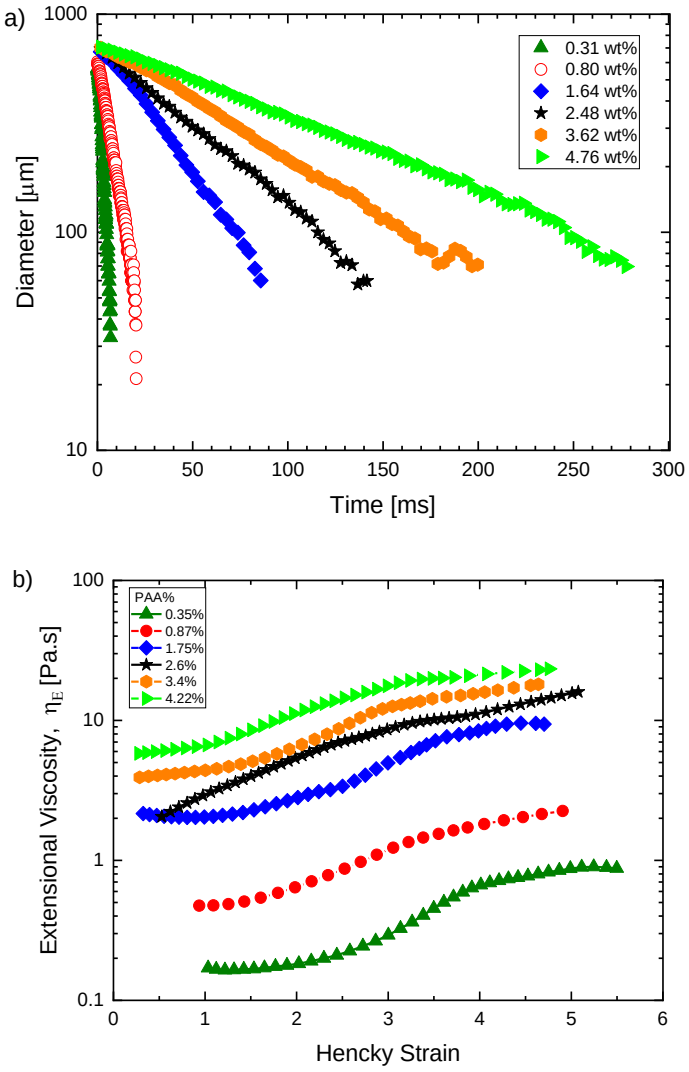

Figure 3. Extensional rheology data of inks with fixed ionomer concentration (3.41 wt.%) for a series of PAA concentration: a) Diameter versus time and b) Extensional viscosity versus Hencky strain.

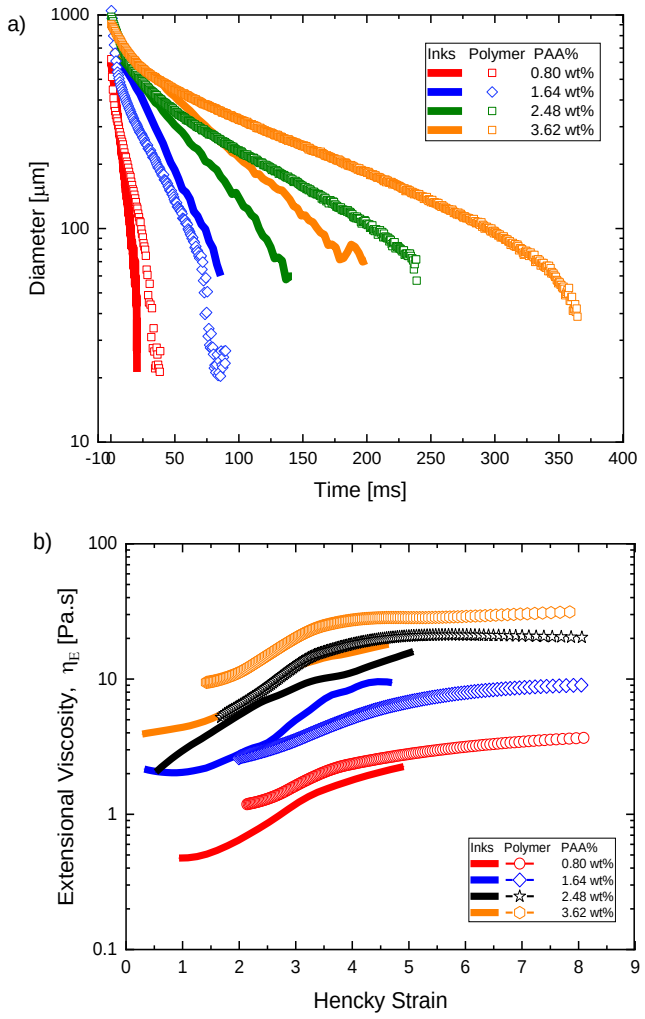

Figure 4. Extensional rheology data comparison between inks and polymers at a fixed ionomer concentration (3.41 wt%) for a series of PAA concentrations: a) Diameter versus time and b) Extensional viscosity versus Hencky strain.

The fiber evolution process in electrospinning is predominantly dictated by the extensional rheological properties of the fluids[18]. To understand the processing behavior of the inks, we characterized their extensional rheology for different PAA concentrations at a fixed ionomer concentration (3.41 wt.%). The diameter decay data for the inks is shown in Figure 3a. The overall lifetime of the filaments increases with increasing PAA concentration, implying an increase in the stability of the ink filaments against capillary break-up. If we examine the decay profiles, all the inks decay linearly at initial times, followed by a weaker exponentially decay, which is a characteristic decay behavior of viscoelastic fluids[41]. The

appearance of an exponential decay region indicates the onset of elastic effects. The ratio of elastic to viscous forces in the filament is described by the dynamic dimensionless Weissenberg number, $Wi \sim \lambda_E \dot{\epsilon}_e$[42], where $\dot{\epsilon}_e$ is the extensional deformation rate in the filament. Elastic forces are found to become more important than viscous forces for Wi greater than a critical value of ~ 0.5, due to a coil-stretch transition of the polymer molecules in solutions[43]. The exponential decay region suggests Weissenberg number of the filaments are greater than 0.5. The characteristic extensional relaxation times of the inks also increase with increasing PAA concentration from 5 ms to 50 ms as shown in the Table 1. The onset of elastic effects (i.e. exponential decay) is leading to an increase in the extensional viscosity (η_E) with increasing Hencky strain (known as strain hardening), as might be expected in all the inks, as shown in Figure 3b. Further, the extensional viscosities at any given strain increase with increasing PAA concentration.

Pt-Vulcan particles are anisotropic in shape with mass fractal dimension of $d_f \sim 1.5$[39]. Dispersions of anisotropically shaped particles (e.g. rod-like particles[44]) have been found to exhibit strain-hardening of their extensional viscosity due to the alignment of the particles along the flow direction and the resulting hydrodynamic interaction between particles that ensues[45–47]. Of course, high molecular weight polymer solutions are well-known to exhibit strain-hardening behavior due to coil-stretching in extensional flow[48]. Therefore, both particles and PAA in the ink are likely contributing to the observed strain-hardening of the extensional viscosity (by flow-induced alignment of the particles and stretching of the polymer coils). However, because the particle concentration has been fixed and only the concentration of PAA has been increased in Figure 3, the observed growth in extensional viscosity and relaxation time is due entirely to changes in PAA concentration. The effect of particles is more clearly observed in the lowest PAA concentration systems where strain hardening of the extensional viscosity was observed even in the absence of a measurable relaxation time of the fluid.

To further understand how PAA-particle interactions in the ink are influencing the strain hardening behavior of the inks, we compared the extensional rheology measurements of the full catalyst inks against polymer-only solutions (PAA + ionomer) at equivalent polymer concentration, where the ionomer was fixed at 3.41 wt.%. The diameter decay data of the polymer-only solutions is compared against the inks in Figure 4a and Figure 4*b*. Both the filament lifetimes and the extensional relaxation times (Table 1) of the polymer solutions increase with increasing concentration, as expected[31]. Previous studies on electrospinning of Nafion/PAA solutions observed improvement in fiber formation transitioning from

beads or beads-and-fibers to uniform fibers with increasing PAA concentration, which is consistent with the observed trend in the extensional relaxation times of the solutions[19]. We observe the extensional relaxation times of the polymer solutions to be larger than that of the full catalyst inks. Additionally, the extensional viscosities of the inks and polymer solutions were compared in terms of Trouton ratio, which is defined as the ratio of extensional viscosity and shear viscosity, $Tr = \eta_E/\eta_s(\dot{\gamma} = \sqrt{3}\dot{\epsilon})$. The Trouton ratio is three (Tr = 3) for simple liquids (i.e. Newtonian fluids) where structural change does not differ between shear and extension. The Trouton ratios at large Hencky strains, where extensional viscosities tend to a plateau, have been evaluated. The corresponding shear viscosities (Figure S4a & S4b) – the viscosities at shear-rates equivalent to the extension rates at large Hencky strains – were used for the evaluations. These were found to be Tr ~ 23 – 37 and Tr ~ 170 – 230 for the inks and the polymer solutions, respectively. The Trouton ratio for both fluids is much greater than three (Tr >> 3), which is consistent with previous studies on polymer solutions and colloidal dispersions, and indicates strong extensional flow-induced structuring in both materials[31,49]. However, the Trouton ratio of polymer solutions is much greater than the inks, by approximately 6x. These comparisons show that the extensibility of the polymer solutions is much greater in the absence of the particles present in the inks.

The observations are similar to a previous finding where pure polyethylene oxide polymer solutions demonstrated enhanced extensional viscosities compared to mixtures with fumed silica dispersions[49]. The reduced extensional viscosities in colloidal mixtures has been attributed to the adsorption of some fraction of the polymer onto the particles. Adsorption onto the surface is likely to restrain the polymer from freely stretching under extensional flow, unlike pure polymer solutions where all the polymer coils would be freely available to stretch under extensional flow field, consequently reducing extensional viscosities. The shear rheology observations of the inks (Figure 2) indicated that the PAA adsorbs onto particles, as discussed previously. Therefore, the reduced extensional viscosities of the inks compared to pure polymer solutions could be attributed to the similar mechanism.

These comparisons of the extensional rheology between inks and pure polymer solutions further indicate the presence of significant interaction between the catalyst particles and the carrier polymer, which is consistent with the shear rheology observations. While the extensional-flow properties of the inks are weaker compared to pure polymer solutions, increasing PAA concentration is overall increasing the extensional-flow properties of the inks. This can be expected to facilitate fiber formation in the electrospinning process, where extensional viscosities enhance the stability of the jet against break-up by

capillary forces. In the following section, we examine how the extensional rheological properties influence the spinnability and fiber morphologies.

Electrospinning

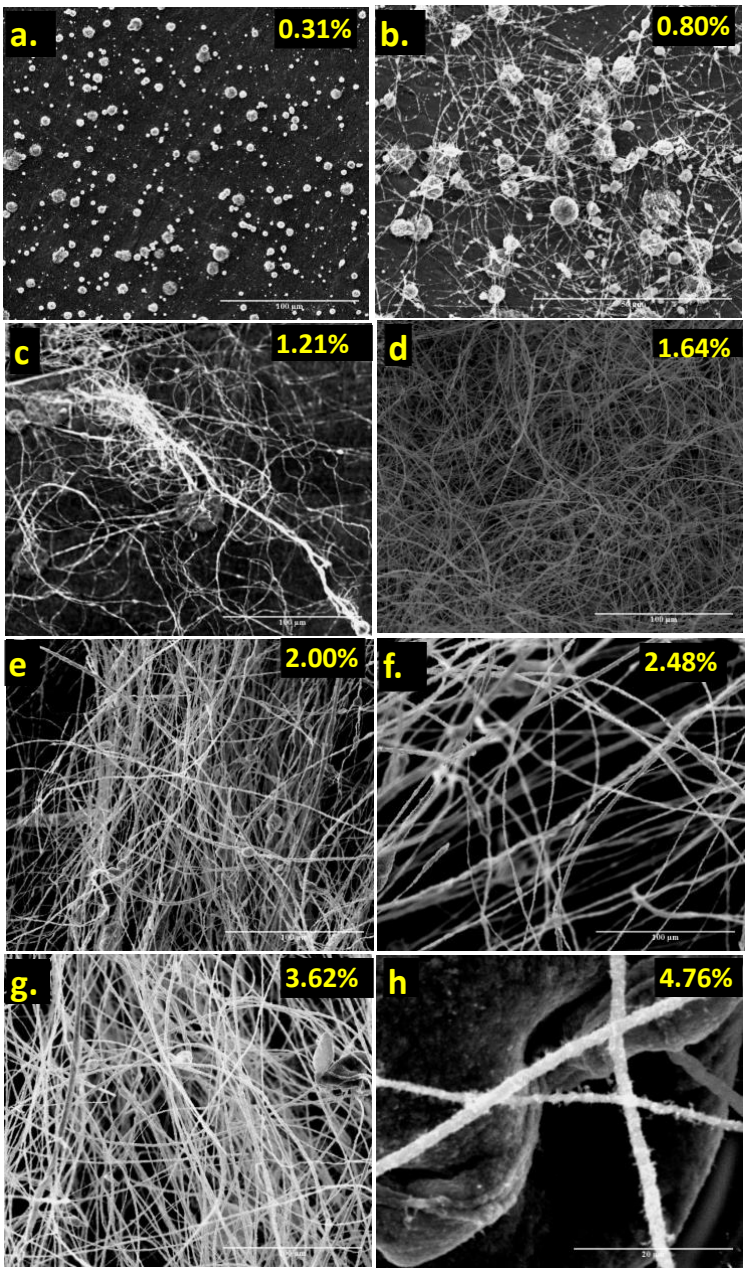

Figure 5. SEM images of electrospun fibers of catalyst inks containing different PAA% concentrations: a) 0.31 wt%, b) 0.80 wt%, c) 1.21 wt%, d) 1.64 wt%, e) 2.00 wt%, f) 2.48 wt%, g) 3.62 wt%, and h) 4.76 wt%.

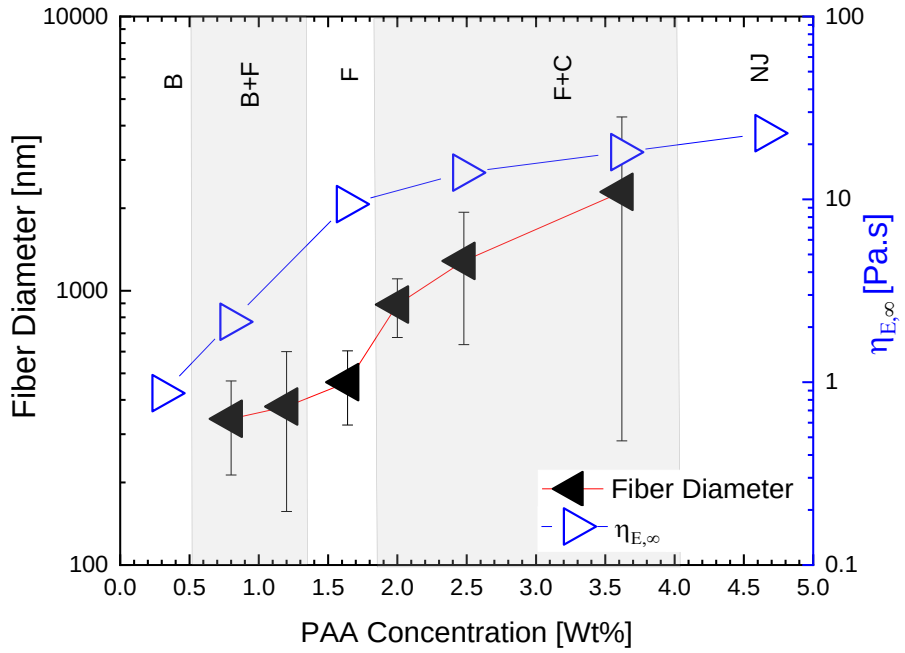

Figure 6. Diameter of electrospun fibers (left axis) and extensional viscosities at large Hencky strain ($\eta_{E,\infty}$) (right axis) as a function of PAA concentration in the ink. The labels on the figure represent concentration regions where different fiber morphologies were observed. These include: beads only (B), beads and fibers (B+F), uniform fibers (F), and fibers and clumps (F+C). NJ implies not jettable.

Electrospinning experiments were conducted on the inks with various PAA concentrations for a fixed ionomer concentration. SEM images of the resulting electrospun fiber morphologies are presented in Figure 5. Fiber morphologies significantly varied based on PAA wt.%. Beads (without any fibers) were observed at the lowest studied PAA concentration of 0.31 wt.%, indicating the formation of the droplets during the jetting process similar to an electro-spraying process (Figure 5a). As the PAA concentration is further increased, a combination of beads and fibers were observed (Figure 5b & Figure 5c). At a PAA concentration of 1.64 wt.%, uniform fibers (without any beads) begin to form (Figure 5d). Increasing PAA concentration beyond 1.64 wt.% resulted in an overall increase in the average diameter of the fibers,

which were found to be ~ 400 nm at 1.64 wt.% PAA, increasing up to 2.3 μm at 3.62 wt.% PAA, as shown in Figure 6. The observed fiber morphological transitions – from only beads to uniform fibers – and variation of the fiber diameter with increasing PAA concentration is similar to several previous studies[17–19,25]. At PAA concentrations ≥ 1.64 wt.%, defects - intermittent clumps of non-dispersed ink material - begin to appear along the fibers (Figure 5e – Figure 5*g*). Beyond 3.62 wt.%, we begin to experience pumping difficulties where large chunks of catalyst are ejected intermittently (Figure 5h).

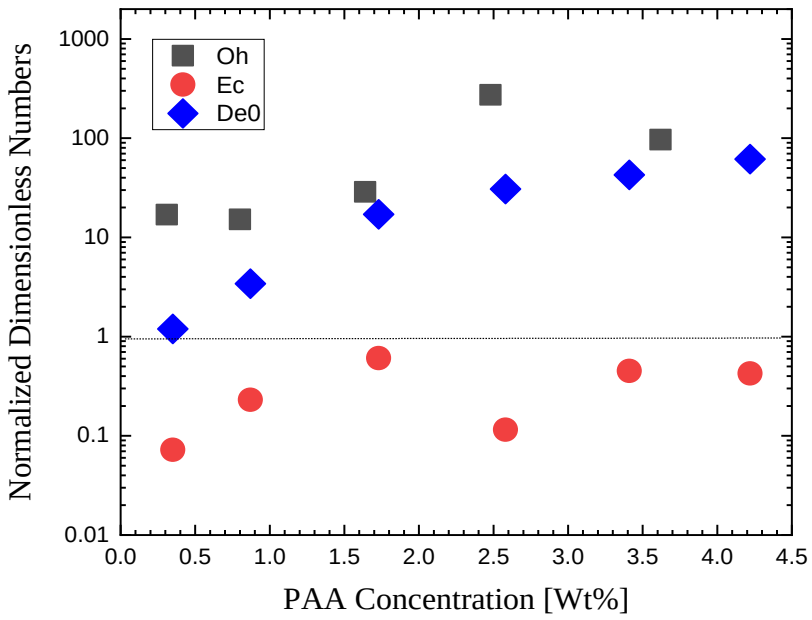

Figure 7. Normalized Dimensionless numbers evaluated for inks for a series of PAA concentration which include: Ohnesorge number, Oh_N = Oh/Oh_c (Oh_c ~ 0.2), Elasticity number, Ec_N = Ec/Ec_c (Ec_c ~ 4.7), and Intrinsic Deborah number, De_{0N} = De_0/ De_{0c} (De_{0c} ~ 1).

To gain insights into mechanism of the evolution of the different fiber morphologies, we compared the ink properties in terms of global dimensionless numbers to understand the relative importance of relevant forces on the overall jet dynamics during electrospinning[42,50]. The ratio of viscous to inertial forces is given by the Ohnesorge number, $Oh \sim \eta_0/\sqrt{\rho\sigma R_0}$, where η_0, ρ and σ are zero-shear viscosity, density, and surface tension of the fluids, respectively, and R_0 is the characteristic length scale of the process. For Oh > 0.2 viscous forces are shown to dominate inertial forces[50]. The ratio of elastic and viscous forces is described by the Elasto-Capillary Number, $Ec \sim \lambda_E\sigma/\eta_0 R_0$, where λ_E and σ are extensional relaxation

time and interfacial tension of the fluid, respectively. For $Ec > Ec_c \sim 4.7$, a critical Elasto-Capillary Number, the elastic forces are found to be more important than viscous forces[50]. The ratio of elastic and inertial forces is given by the intrinsic Deborah number, $De_0 \sim \sqrt{\lambda_E^2 \sigma / \rho R_0^3}$. For $De_0 > De_{0c} \sim 1$ the elastic effects are known to dominate inertia[50]. These have been evaluated for all the inks using radius of the nozzle (R_0) as the characteristic length of the process. For η_0, as all the inks predominantly shear thin (SI. 3), the viscosity values corresponding to shear-rates in the nozzle ($\dot{\gamma}_0 \sim v_0/R_0 \sim 4.5\ s^{-1}$, where $v_0 \sim Q_0/\pi R_0^2$) were used for estimations.

The evaluated global dimensionless numbers were compared as a function of PAA concentration in Figure 7. To easily visualize the dominant forces, the global dimensionless numbers were normalized by their respective critical values as $Oh_N = Oh/Oh_c$, $De_{0N} \sim De_0/De_{0c}$, and $Ec_N = Ec/Ec_c$. We can observe that for all PAA concentrations, $Oh_N > De_N > 1$ and $Ec_N < 1$. This indicates that overall jet dynamics are predominantly controlled by the viscous forces, followed by elastic forces, and least by inertia. The normalized elasticity number $Ec_N < 1$ for all cases implies that the inks are mildly elastic at all PAA concentrations. This analysis thus suggests that increasing PAA concentration is increasing the viscosity of the inks more significantly than it is increasing the elasticity of the inks. This may be undesired in the electrospinning process as it could cause flow difficulties and affect the fiber morphologies. Previous studies on the jet evolution behavior of viscoelastic fluids during the electrospinning process have observed strain-hardening of the fluids due to acceleration of the jet during the initial stages of the jet evolution process[51,52]. All the inks can similarly undergo strain-hardening (as exhibited in extensional rheology) for Weissenberg number of the jets $Wi > 0.5$ during the acceleration stages which is plausible as the extension rates in electrospinning are known to be generally very high[51]. The increase in the extensional viscosities due to strain hardening of the inks during the jet evolution can enhance the stability of the jet against break-up.

To quantitatively relate the extensional rheological properties of the inks and the fiber morphologies, the extensional rates of the jets as well as the extensional viscosities at the corresponding extension rates would need to be determined. However, we can qualitatively relate the evolution of different fiber morphologies to the trend in their extensional viscosities at the large Hencky strains ($\eta_{E,\infty}$) they approach due to strain-hardening, as summarized in Figure 6. Because the $\eta_{E,\infty}$ of the inks increase with increasing PAA concentration, we presume that the stability of the jets as a function of PAA concentration would

also increase. The beads-only morphology at 0.31 wt% is likely due to insufficient $\eta_{E,\infty}$ of the inks to completely suppress inertial forces and prevent break-up of the jet into droplets. The evolution of beads and fibers morphology observed at PAA concentrations of 0.80 - 1.21 wt.% could be due to a moderate increase in the $\eta_{E,\infty}$ of the inks. However, this only partially stabilizes the jet against inertia forces that are shown to drive bead formation along the filaments. Such morphology is common for weakly viscoelastic fluids[2,58,42]. At 1.64 wt.% PAA the inertial forces are completely suppressed/resisted due to a sufficient increase in $\eta_{E,\infty}$ and hence the uniform fibers.

The appearance of embedded clumps in the fibers (Figure 5h) for PAA concentrations ≥ 1.64 wt.% is likely due to flow instabilities in the nozzle and their propagation along the jet. While increasing PAA concentration increases both the elasticity and the viscosity of the inks, their Oh_N is consistently larger than De_{0N} and Ec_N, suggesting that the inks are predominantly viscous. This suggests viscous effects could dominate the flow in the nozzle rather than elasticity. Though elastic effects are known to lead to instabilities in pipe flows[24,54], the evaluated Weissenberg numbers in the nozzle are less than 0.5. The estimated Wi based on pump flow rates $Wi_z \sim \dot{\gamma}_0 \lambda_E$ for 3.62 wt.% and 4.76 wt.% PAA cases were found to be $Wi_z \sim 0.12$ and 0.17, respectively. Therefore, the formation of defective fibers is mostly likely to due to the significant viscosities of the inks that lead to an unstable flow in the nozzle.

The results demonstrate that PAA concentration significantly impacts the fiber morphologies, consistent with previous findings[55]. Uniform fibers were obtained at an intermediate PAA concentration suggesting an optimal viscoelasticity of the inks. The analysis of the ink properties in terms of relevant dimensionless numbers indicated the inks are mildly elastic ($Ec_N < 1$) where increasing PAA concentration increases the inks' viscosity in addition to their elasticity. As a result, uniform fibers evolve over a narrow range of PAA concentration, between 1.21 wt.% to 2.00 wt.%, wherein the inks are likely sufficiently elastic, but not too viscous, to generate a stable flow.

Performance

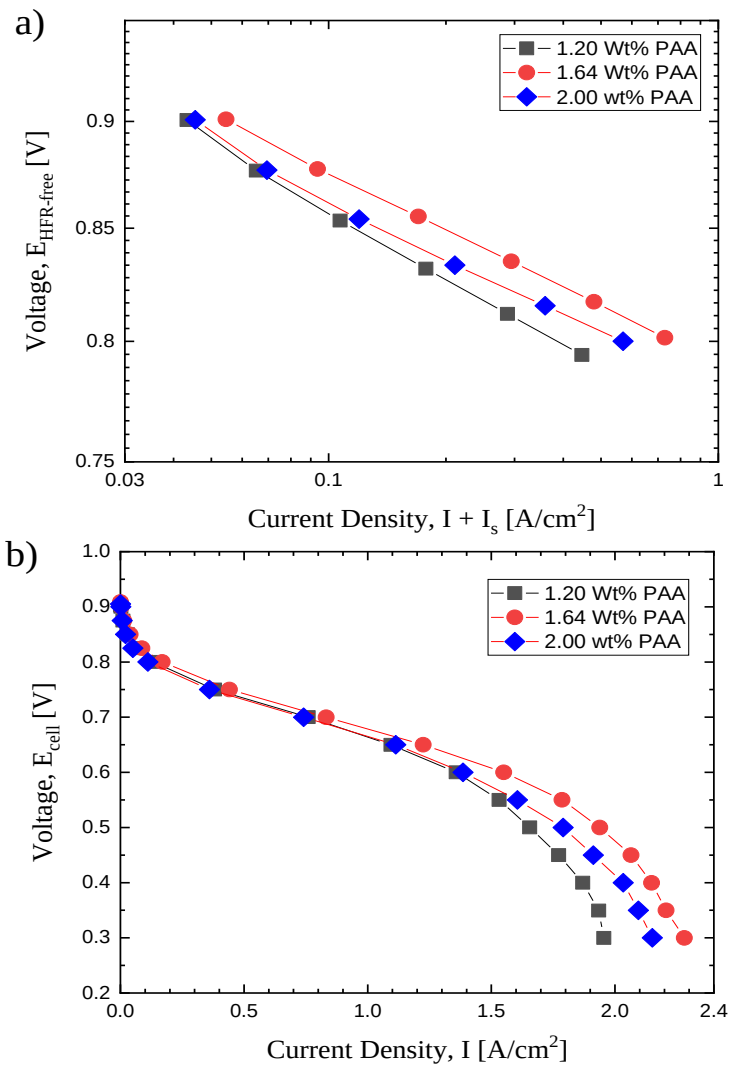

Figure 8. Electrochemical measurements of nanofiber electrodes fabricated with 1.20, 1.64, and 2.00 wt.% PAA tested in 5 cm^2 MEAs at a Pt target loading of 0.10 $mgPt.cm^{-2}$. (a) I/V curves obtained in H_2/O_2 at 80C, 150 kPa and 100% RH. (b) H_2/Air polarization curves obtained at 80°C, 150 kPa and 100% RH.

Lastly, we examine the impact of PAA content and fiber morphology of the catalyst layer on fuel cell performance. For the performance comparison, we focus on three catalyst layers representative of different fiber morphologies that were fabricated from catalyst inks containing 1.20 wt.%, 1.64 wt.% and 2.00 wt.% PAA. Two of these cases, though defective, had enough of a fraction of fibers feasible to fabricate and

test MEA performance. The hydrogen crossover corrected current densities obtained between 0.75 V – OCV from the H_2/O_2 V-I curves are presented in Figure 8a. The data clearly shows improved oxygen reduction reaction (ORR) kinetics for the 1.64 wt.% PAA case, with an ORR mass activity of 487 mA/mgPt, compared to mass activities of 371 mA/mgPt and 403 mA/mgPt for the 1.20 wt.% and 2.00 wt.% PAA cases, respectively. The electrochemically accessible surface area (ECSA) was determined from the HUPD region from cyclic voltammograms (Figure S5 in SI). The 1.64 wt.% PAA case has a higher ECSA of 61.4 m^2/g compared to ECSAs of 1.20 wt.% and 2.00 wt.% PAA which are 45 m^2/g and 47 m^2/g, respectively. The 1.64 wt.% PAA case also demonstrates higher performance across a range of current density, as seen in the H_2/Air polarization curves of Figure 8b.

The mass activities of the 1.2 wt% and 2.0 wt% PAA nanofiber electrodes are 76% and 83% of the mass activity of the 1.67 wt% PAA nanofiber electrode. This is consistent with the differences in ECSA, where the 1.2 wt% and 2.0 wt% PAA nanofiber electrodes had 73% and 77% of the ECSA of the 1.67 wt% PAA nanofiber electrodes. This indicates that the performance differences most likely stem from differences in catalyst utilization/ accessibility. Variation in ionomer distribution and ionomer coverage on Pt nanoparticles and the carbon support are a likely explanation and have been shown elsewhere[30]. The bead/clumps in the 1.2 wt% and 2.0 wt% PAA nanofiber electrodes may also be contributing to the lower Pt accessibility. The irregularities of these areas could be leading to Pt/Vu particles that are electronically or protonically isolated and unable to contribute electrochemically.

The differences in the ink microstructure shed some light on differences in the internal structure of the fibers as a function of PAA concentration, i.e. the catalyst agglomerated structure and the amount of excess/free PAA content (not interacting with particles). The agglomerated structure of the inks reduced with increasing PAA, significantly when increasing from 1.20 wt.% and 1.64 wt.% where the equilibrium microstructure transitioned from gel-like (percolated network of particles) to liquid-like (isolated particles/agglomerates). Further reduction of the agglomerates with increasing PAA beyond 1.64 wt.% appeared to be less significant. We can expect qualitatively similar trends in particle structure in the fibers as function of PAA as in the inks, though we would expect this to be less in magnitude due to the partial break-down of the agglomerated structure by the deformations during the electrospinning process. A decrease in the agglomerated catalyst was previously found increase the electrode ECSA, and thus the device performance, suggesting the same effect may be occurring here[56]. Therefore, the observed increase

in ECSA and performance with the increase in PAA from 1.20 and 1.64 wt.% is consistent with the catalyst agglomerated structure in the ink.

However, the reduction in ECSA and performance with further increase in PAA concentration from 1.64 wt.% to 2.00 wt.% is likely due to an excess of PAA in the fibers as suggested by the rheological behavior. Above 1.64 wt.%, the viscoelasticity of the inks was found to be dominated by the excess PAA concentration rather than by the changes in the particle agglomerated structure (Figure 2). Excess PAA in the fibers could reduce the mass transport (gas/water) to/from the catalyst sites and reduce the catalyst utilization/ECSA in the fibers, thereby negatively affecting performance[56]. Thus, the excess PAA, in combination with the non-uniform (fiber and clumps) fiber morphology, likely caused the reduction in ECSA and performance in the 2.00 wt.% PAA case. In addition to these factors (defective fiber morphologies and reduced porosity), inferior ion-conducting properties of PAA relative to Nafion may also play a role in the performance reduction at these high PAA concentrations as indicated in previous studies, both for spray-coated[7] and nanofiber electrodes[3].

The performance comparisons show maximum fuel cell performance at an optimal PAA concentration of 1.64 wt.% which corresponds to the catalyst layer with uniform fiber morphology, minimal catalyst agglomerates, and less amounts of free (non-adsorbing) PAA in the electrode. The inferences drawn of the internal structure of the fibers to rationalize the performance differences were primarily based on the rheology observations that capture bulk changes in the ink microstructure. The deformation of the inks during the electrospinning and drying processes could influence the internal structure of the fibers and thus the local environment of the catalyst, (the three-phase interface) which controls fuel cell performance. In a separate study to confirm the relationship between the observations of ink microstructure and performance, and to gain more insights into the performance mechanisms we further examined the internal structure of the fibers – the ionomer distribution in the nanofibers and the local ionomer-platinum interactions – and its impact on sulfonate coverage on the catalyst and proton accessibility.[30] The results from these combined studies provide insights into structure and function of electrospun nanofiber electrodes and will guide future nanofiber electrode R&D.

Conclusions

In conclusion, the study shows that carrier-polymer not only facilitates the formation of uniform fibers, but its interaction with the catalyst particles can significantly influence fuel cell performance. Particularly, a reduction in the catalyst agglomerates by the carrier polymer can have a positive effect on the performance of fuel cells. The PAA, along with the ionomer, stabilized the particles (via electrosteric stabilization) against agglomeration by adsorbing onto their surface. However, beyond a certain concentration (> 1.64 wt.%), PAA predominantly remained as excess free polymer in the bulk because of reduction in the free surface area of the particles for further PAA adsorption. We also found that PAA overall enhances the extensional viscosities of inks, as expected, but its interaction with particles appears to reduce their extensional viscosities relative to pure polymer solutions, owing to their adsorption onto the catalyst surface that restrains the polymer from fully stretching under extensional flow. The enhancement of the extensional viscosities of the inks by PAA promoted the evolution of uniform nanofibers by suppressing the formation of bead morphologies. However, at large PAA concentrations, significant increase in shear viscosities resulted in defective fibers (beads embedded with clumps). Electrochemical performance comparisons between three nanofiber catalyst layers with different PAA concentrations showed maximum performance at an optimal PAA concentration that provides a combination of both a decrease in the agglomerated structure of the catalyst and improvement in fiber uniformity. The findings from this study contribute to a more rational approach to the fabrication of nanofiber electrodes and show that an understanding of the polymer-particle interactions is necessary to optimize ink formulation to control fiber formation and create optimal electrode structure for fuel cell performance.

Supporting Information

Schematics of drip on a substrate capillary breakup extensional rheometer and electrospinning experimental set-up; tan δ and non-linear viscoelastic properties (strain softening and strain thinning exponents) as function of PAA concentration in the inks; steady-shear rheology of inks and PAA solutions at different PAA concentrations; cyclic voltammogram results for the determination of the electrochemically active catalyst surface area of the nanofiber electrodes at different PAA concentrations.

Author Information

ORCID

Sunilkumar Khandavalli: 0000-0003-3179-5718

Sadia Kabir: 0000-0002-5064-7916

Samrat Sur: 0000-0003-3214-6365

Jonathan P. Rothstein: 0000-0002-9344-1133

Kenneth C. Neyerlin: 0000-0002-6753-9698

Scott A. Mauger: 0000-0003-2787-5029

Michael Ulsh: 0000-0003-3725-8032

Acknowledgments

This work was authored by Alliance for Sustainable Energy, LLC, the manager and operator of the National Renewable Energy Laboratory for the U.S. Department of Energy (DOE) under Contract No. DE-AC36-08GO28308. Funding provided by U.S. Department of Energy, Office of Energy Efficiency

and Renewable, Advanced Manufacturing Office and Hydrogen and Fuel Cell Technologies Office. The views expressed in the article do not necessarily represent the views of the DOE or the U.S. Government. The U.S. Government retains and the publisher, by accepting the article for publication, acknowledges that the U.S. Government retains a nonexclusive, paid-up, irrevocable, worldwide license to publish or reproduce the published form of this work, or allow others to do so, for U.S. Government purposes.

Table 1. Extensional relaxation times of inks and PAA solutions (with 3.41 wt.% ionomer) for a series of different PAA concentrations.

	Inks	**Polymer solutions**
PAA wt.%	**Relaxation Time [ms]**	**Relaxation Time [ms]**
0.80	2	5
1.64	10	12
2.48	18	37
3.62	25	2

References

(1) Litster, S.; McLean, G. PEM Fuel Cell Electrodes. *J. Power Sources* **2004**, *130* (1–2), 61–76. https://doi.org/10.1016/j.jpowsour.2003.12.055.

(2) Holdcroft, S. Fuel Cell Catalyst Layers: A Polymer Science Perspective. *Chem. Mater.* **2014**, *26* (1), 381–393. https://doi.org/10.1021/cm401445h.

(3) Zhang, W.; Pintauro, P. N. High-Performance Nanofiber Fuel Cell Electrodes. *ChemSusChem* **2011**, *4* (12), 1753–1757. https://doi.org/10.1002/cssc.201100245.

(4) Martin, S.; Garcia-Ybarra, P. L.; Castillo, J. L. Electrospray Deposition of Catalyst Layers with Ultra-Low Pt Loadings for PEM Fuel Cells Cathodes. *J. Power Sources* **2010**, *195* (9), 2443–2449. https://doi.org/10.1016/j.jpowsour.2009.11.092.

(5) Debe, M. K.; Schmoeckel, A. K.; Vernstrom, G. D.; Atanasoski, R. High Voltage Stability of Nanostructured Thin Film Catalysts for PEM Fuel Cells. *J. Power Sources* **2006**, *161* (2), 1002–1011. https://doi.org/10.1016/j.jpowsour.2006.05.033.

(6) Slack, J.; Halevi, B.; McCool, G.; Li, J.; Pavlicek, R.; Wycisk, R.; Mukerjee, S.; Pintauro, P. Electrospun Fiber Mat Cathode with Platinum-Group-Metal-Free Catalyst Powder and Nafion/PVDF Binder. *ChemElectroChem* **2018**, *5* (12), 1537–1542. https://doi.org/10.1002/celc.201800283.

(7) Brodt, M.; Han, T.; Dale, N.; Niangar, E.; Wycisk, R.; Pintauro, P. Fabrication, in-Situ Performance, and Durability of Nanofiber Fuel Cell Electrodes. *J. Electrochem. Soc.* **2015**, *162* (1), F84–F91. https://doi.org/10.1149/2.0651501jes.

(8) Shui, J.; Chen, C.; Grabstanowicz, L.; Zhao, D.; Liu, D. J. Highly Efficient Nonprecious Metal Catalyst Prepared with Metal-Organic Framework in a Continuous Carbon Nanofibrous Network. *Proc. Natl. Acad. Sci. U. S. A.* **2015**, *112* (34), 10629–10634. https://doi.org/10.1073/pnas.1507159112.

(9) Kabir, S.; Medina, S.; Wang, G.; Bender, G.; Pylypenko, S.; Neyerlin, K. C. Improving the Bulk Gas Transport of Fe-N-C Platinum Group Metal-Free Nanofiber Electrodes via Electrospinning

for Fuel Cell Applications. *Nano Energy* **2020**, *73*, 104791. https://doi.org/10.1016/j.nanoen.2020.104791.

(10) Kotera, S.; Watabe, H.; Fujii, K.; Terada, I.; Matsubara, C.; Uyama, H. Study on the Cathode Fabricated by Spinning Process and Its Performance in PEFC. *ECS Trans.* **2019**, *25* (1), 821–830. https://doi.org/10.1149/1.3210635.

(11) Waldrop, K.; Wycisk, R.; Pintauro, P. N. Application of Electrospinning for the Fabrication of Proton-Exchange Membrane Fuel Cell Electrodes. *Current Opinion in Electrochemistry*. Elsevier B.V. June 1, 2020, pp 257–264. https://doi.org/10.1016/j.coelec.2020.03.007.

(12) Teo, W. E.; Ramakrishna, S. A Review on Electrospinning Design and Nanofibre Assemblies. *Nanotechnology* **2006**, *17* (14), R89–R106. https://doi.org/10.1088/0957-4484/17/14/R01.

(13) Cavaliere, S.; Subianto, S.; Savych, I.; Jones, D. J.; Rozière, J. Electrospinning: Designed Architectures for Energy Conversion and Storage Devices. *Energy and Environmental Science*. Royal Society of Chemistry December 22, 2011, pp 4761–4785. https://doi.org/10.1039/c1ee02201f.

(14) Reneker, D. H.; Yarin, A. L. Electrospinning Jets and Polymer Nanofibers. *Polymer (Guildf).* **2008**, *49* (10), 2387–2425. https://doi.org/10.1016/j.polymer.2008.02.002.

(15) Shenoy, S. L.; Bates, W. D.; Frisch, H. L.; Wnek, G. E. Role of Chain Entanglements on Fiber Formation during Electrospinning of Polymer Solutions: Good Solvent, Non-Specific Polymer-Polymer Interaction Limit. *Polymer (Guildf).* **2005**, *46* (10), 3372–3384. https://doi.org/10.1016/j.polymer.2005.03.011.

(16) Gupta, P.; Wilkes, G. L. Some Investigations on the Fiber Formation by Utilizing a Side-by-Side Bicomponent Electrospinning Approach. *Polymer (Guildf).* **2003**, *44* (20), 6353–6359. https://doi.org/10.1016/S0032-3861(03)00616-5.

(17) McKee, M. G.; Wilkes, G. L.; Colby, R. H.; Long, T. E. Correlations of Solution Rheology with Electrospun Fiber Formation of Linear and Branched Polyesters. *Macromolecules* **2004**, *37* (5), 1760–1767. https://doi.org/10.1021/ma035689h.

(18) Yu, J. H.; Fridrikh, S. V.; Rutledge, G. C. The Role of Elasticity in the Formation of Electrospun Fibers. *Polymer (Guildf).* **2006**, *47* (13), 4789–4797. https://doi.org/10.1016/j.polymer.2006.04.050.

(19) Chen, H.; Snyder, J. D.; Elabd, Y. A. Electrospinning and Solution Properties of Nafion and Poly (Acrylic Acid). *Society* **2008**, 128–135.

(20) Bajon, R.; Balaji, S.; Guo, S. M. Electrospun Nafion Nanofiber for Proton Exchange Membrane Fuel Cell Application. *J. Fuel Cell Sci. Technol.* **2009**, *6* (3), 0310041–0310046. https://doi.org/10.1115/1.3005577.

(21) Slack, J. J.; Gumeci, C.; Dale, N.; Parrondo, J.; Macauley, N.; Mukundan, R.; Cullen, D.; Sneed, B.; More, K.; Pintauro, P. N. Nanofiber Fuel Cell MEAs with a PtCo/C Cathode. *J. Electrochem. Soc.* **2019**, *166* (7), F3202–F3209. https://doi.org/10.1149/2.0151907jes.

(22) Kabir, S.; Myers, D. J.; Kariuki, N.; Park, J.; Wang, G.; Baker, A.; Macauley, N.; Mukundan, R.; More, K. L.; Neyerlin, K. C. Elucidating the Dynamic Nature of Fuel Cell Electrodes as a Function of Conditioning: An Ex Situ Material Characterization and in Situ Electrochemical Diagnostic Study. *ACS Appl. Mater. Interfaces* **2019**, *11* (48), 45016–45030. https://doi.org/10.1021/acsami.9b11365.

(23) Li, J.; Brüller, S.; Sabarirajan, D. C.; Ranjbar-Sahraie, N.; Sougrati, M. T.; Cavaliere, S.; Jones, D.; Zenyuk, I. V.; Zitolo, A.; Jaouen, F. Designing the 3D Architecture of PGM-Free Cathodes for H2/Air Proton Exchange Membrane Fuel Cells. *ACS Appl. Energy Mater.* **2019**, *2* (10), 7211–7222. https://doi.org/10.1021/acsaem.9b01181.

(24) Petrie, C. J. S.; Denn, M. M. Instabilities in Polymer Processing. *AIChE Journal*. John Wiley & Sons, Ltd March 1, 1976, pp 209–236. https://doi.org/10.1002/aic.690220202.

(25) Chen, G. H.; Kelly, D.; Shine, A.; Liu, Z.; Wang, L.; Bliznakov, S.; Rafailovich, M. Electrospinning Deposition of Poly(Acrylic Acid): Platinum/Carbon Catalyst Ink to Enhance Polymer Electrolyte Membrane Fuel Cell Performance. *MRS Commun.* **2019**, *9* (4), 1343–1348. https://doi.org/10.1557/mrc.2019.144.

(26) Holdcroft, S. Fuel Cell Catalyst Layers: A Polymer Science Perspective. *Chem. Mater.* **2014**, *26*

(1), 381–393. https://doi.org/10.1021/cm401445h.

(27) Hong, S.; Hou, M.; Zhang, H.; Jiang, Y.; Shao, Z.; Yi, B. A High-Performance PEM Fuel Cell with Ultralow Platinum Electrode via Electrospinning and Underpotential Deposition. *Electrochim. Acta* **2017**, *245*, 403–409. https://doi.org/10.1016/j.electacta.2017.05.066.

(28) Si, D.; Zhang, S.; Huang, J.; Wang, C.; Liu, Y.; Zhang, J. Electrochemical Characterization of Pre-Conditioning Process of Electrospun Nanofiber Electrodes in Polymer Electrolyte Fuel Cells. *Fuel Cells* **2018**, *18* (5), 576–585. https://doi.org/10.1002/fuce.201700209.

(29) Hatzell, K. B.; Dixit, M. B.; Berlinger, S. A.; Weber, A. Z. Understanding Inks for Porous-Electrode Formation. *J. Mater. Chem. A* **2017**, *5* (39), 20527–20533. https://doi.org/10.1039/c7ta07255d.

(30) Kabir, S.; Cleve, T. Van; Khandavalli, S.; Medina, S.; Pylypenko, S.; Mauger, S. A.; Ulsh, M.; Neyerlin, K. C. Towards Optimizing Electrospun Nanofiber Fuel Cell Catalyst Layers: Microstructure and Pt-Accessibility. Submitted to ACS Applied Energy Materials (Under Review) 2021.

(31) Sur, S.; Rothstein, J. Drop Breakup Dynamics of Dilute Polymer Solutions: Effect of Molecular Weight, Concentration, and Viscosity. *J. Rheol.* **2018**, *62* (5), 1245–1259. https://doi.org/10.1122/1.5038000.

(32) Clasen, C.; Plog, J. P.; Kulicke, W.-M.; Owens, M.; Macosko, C.; Scriven, L. E.; Verani, M.; McKinley, G. H. How Dilute Are Dilute Solutions in Extensional Flows? *J. Rheol.* **2006**, *50* (6), 849–881. https://doi.org/10.1122/1.2357595.

(33) Vazquez, G.; Alvarez, E.; Navaza, J. M. Surface Tension of Alcohol + Water from 20 to 50 °C. *J. Chem. Eng. Data* **1995**, *40* (3), 611–614. https://doi.org/10.1021/je00019a016.

(34) Papageorgiou, D. T. On the Breakup of Viscous Liquid Threads. *Phys. Fluids* **1995**, *7* (7), 1529–1544. https://doi.org/10.1063/1.868540.

(35) Entov, V. M.; Hinch, E. J. Effect of a Spectrum of Relaxation Times on the Capillary Thinning of a Filament of Elastic Liquid. *J. Nonnewton. Fluid Mech.* **1997**, *72* (1), 31–53.

https://doi.org/10.1016/S0377-0257(97)00022-0.

(36) Larson, R. G. *The Structure and Rheology of Complex Fluids*; Larson, R. G., Ed.; Oxford University Press Inc.: New York, 1999.

(37) Mewis, J.; Wagner, N. J. *Colloidal Suspension Rheology*; Cambridge University Press: Cambridge, 2011.

(38) Hoogeveen, N. G.; Cohen Stuart, M. A.; Fleer, G. J. Can Charged (Block Co)Polymers Act as Stabilisers and Flocculants of Oxides? *Colloids Surfaces A Physicochem. Eng. Asp.* **1996**, *117* (1–2), 77–88. https://doi.org/10.1016/0927-7757(96)03699-0.

(39) Khandavalli, S.; Park, J. H.; Kariuki, N. N.; Myers, D. J.; Stickel, J. J.; Hurst, K.; Neyerlin, K. C.; Ulsh, M.; Mauger, S. A. Rheological Investigation on the Microstructure of Fuel Cell Catalyst Inks. *ACS Appl. Mater. Interfaces* **2018**, *10* (50), 43610–43622. https://doi.org/10.1021/acsami.8b15039.

(40) Liu, Y.; Murphy, M.; Baker, D.; Gu, W.; Ji, C.; Jorne, J.; Gasteiger, H. A. Determination of Electrode Sheet Resistance in Cathode Catalyst Layer by AC Impedance. *ECS Trans.* **2019**, *11* (1), 473–484. https://doi.org/10.1149/1.2780961.

(41) Anna, S. L.; McKinley, G. H. Elasto-Capillary Thinning and Breakup of Model Elastic Liquids. *J. Rheol.* **2001**, *45* (1), 115. https://doi.org/10.1122/1.1332389.

(42) Mckinley, G. H. Dimensionless Groups For Understanding Free Surface Flows of Complex Fluids. In *Soc. Rheol. Bull*; 2005; Vol. 2005, pp 6–9.

(43) Keller, A.; Odell, J. A. The Extensibility of Macromolecules in Solution; A New Focus for Macromolecular Science. *Colloid Polym. Sci.* **1985**, *263* (3), 181–201. https://doi.org/10.1007/BF01415506.

(44) Ma, A. W. K.; Chinesta, F.; Tuladhar, T.; Mackley, M. R. Filament Stretching of Carbon Nanotube Suspensions. *Rheol. Acta* **2008**, *47* (4), 447–457. https://doi.org/10.1007/s00397-007-0247-y.

(45) Lang, C.; Hendricks, J.; Zhang, Z.; Reddy, N. K.; Rothstein, J. P.; Lettinga, M. P.; Vermant, J.; Clasen, C. Effects of Particle Stiffness on the Extensional Rheology of Model Rod-like Nanoparticle Suspensions. *Soft Matter* **2019**, *15* (5), 833–841. https://doi.org/10.1039/c8sm01925h.

(46) Shaqfeh, E. S. G.; Fredrickson, G. H. The Hydrodynamic Stress in a Suspension of Rods. *Phys. Fluids A* **1990**, *2* (1), 7–24. https://doi.org/10.1063/1.857683.

(47) Batchelor, G. K. The Stress Generated in a Non-Dilute Suspension of Elongated Particles by Pure Straining Motion. *J. Fluid Mech.* **1971**, *46* (4), 813–829. https://doi.org/10.1017/S0022112071000879.

(48) Dinic, J.; Sharma, V. Power Laws Dominate Shear and Extensional Rheology Response and Capillarity-Driven Pinching Dynamics of Entangled Hydroxyethyl Cellulose (HEC) Solutions. *Macromolecules* **2020**, *53* (9), 3424–3437. https://doi.org/10.1021/acs.macromol.0c00077.

(49) Khandavalli, S.; Rothstein, J. P. Extensional Rheology of Shear-Thickening Fumed Silica Nanoparticles Dispersed in an Aqueous Polyethylene Oxide Solution. *J. Rheol.* **2014**, *58* (2), 411–431. https://doi.org/10.1122/1.4864620.

(50) Clasen, C.; Phillips, P. M.; Palangetic, L.; Vermant, and J. Dispensing of Rheologically Complex Fluids: The Map of Misery. *AIChE J.* **2012**, *58* (10), 3242–3255. https://doi.org/10.1002/aic.13704.

(51) Wang, Y.; Hashimoto, T.; Li, C. C.; Li, Y. C.; Wang, C. Extension Rate of the Straight Jet in Electrospinning of Poly(N-Isopropyl Acrylamide) Solutions in Dimethylformamide: Influences of Flow Rate and Applied Voltage. *J. Polym. Sci. Part B Polym. Phys.* **2018**, *56* (4), 319–329. https://doi.org/10.1002/polb.24544.

(52) Helgeson, M. E.; Grammatikos, K. N.; Deitzel, J. M.; Wagner, N. J. Theory and Kinematic Measurements of the Mechanics of Stable Electrospun Polymer Jets. *Polymer (Guildf).* **2008**, *49* (12), 2924–2936. https://doi.org/10.1016/j.polymer.2008.04.025.

(53) Bhat, P. P.; Appathurai, S.; Harris, M. T.; Pasquali, M.; McKinley, G. H.; Basaran, O. A. Formation of Beads-on-a-String Structures during Break-up of Viscoelastic Filaments. *Nat. Phys.*

2010, *6* (8), 625–631. https://doi.org/10.1038/nphys1682.

(54) Larson, R. G. Instabilities in Viscoelastic Flows. *Rheologica Acta*. Steinkopff-Verlag May 1992, pp 213–263. https://doi.org/10.1007/BF00366504.

(55) Chen, G. H.; Kelly, D.; Shine, A.; Liu, Z.; Wang, L.; Bliznakov, S.; Rafailovich, M. Electrospinning Deposition of Poly(Acrylic Acid): Platinum/Carbon Catalyst Ink to Enhance Polymer Electrolyte Membrane Fuel Cell Performance. *MRS Commun.* **2019**, *9* (4), 1343–1348. https://doi.org/10.1557/mrc.2019.144.

(56) Wang, M.; Park, J. H.; Kabir, S.; Neyerlin, K. C.; Kariuki, N. N.; Lv, H.; Stamenkovic, V. R.; Myers, D. J.; Ulsh, M.; Mauger, S. A. Impact of Catalyst Ink Dispersing Methodology on Fuel Cell Performance Using In-Situ X-Ray Scattering. *ACS Appl. Energy Mater.* **2019**, *2* (9), 6417–6427. https://doi.org/10.1021/acsaem.9b01037.

TOC Figure